



## **Fe and Cr phase separation in super and hyper duplex stainless steel plates and welds after very short aging times**

Downloaded from: <https://research.chalmers.se>, 2025-12-04 20:04 UTC

Citation for the original published paper (version of record):

A Hosseini, V., Thuvander, M., Lindgren, K. et al (2021). Fe and Cr phase separation in super and hyper duplex stainless steel plates and welds after very short aging times. *Materials and Design*, 210. <http://dx.doi.org/10.1016/j.matdes.2021.110055>

N.B. When citing this work, cite the original published paper.



# Fe and Cr phase separation in super and hyper duplex stainless steel plates and welds after very short aging times



Vahid A Hosseini<sup>a,\*</sup>, Mattias Thuvander<sup>b</sup>, Kristina Lindgren<sup>b</sup>, James Oliver<sup>c</sup>, Nicklas Folkesson<sup>d</sup>, Daniel Gonzalez<sup>e</sup>, Leif Karlsson<sup>a</sup>

<sup>a</sup> Department of Engineering Science, University West, SE-461 86 Trollhättan, Sweden

<sup>b</sup> Department of Physics, Chalmers University of Technology, SE-412 96 Gothenburg, Sweden

<sup>c</sup> Outokumpu Stainless AB, SE-774 41 Avesta, Sweden

<sup>d</sup> ESAB AB, SE-417 55 Göteborg, Sweden

<sup>e</sup> Bodycote, SE-735 23 Surahammar, Sweden

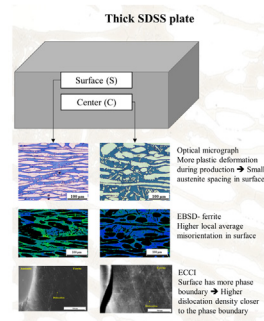
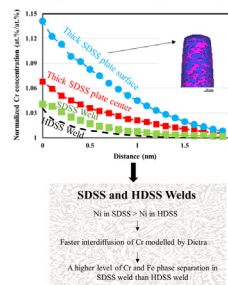
## HIGHLIGHTS

- Plate showed more Cr and Fe phase separation, increase in ferrite microhardness, and drop in toughness compared to the welds.
- Plate-surface with smaller austenite spacing and higher level misorientation and mean angular deviation had more phase separation than plate-center.
- Higher Ni content super duplex stainless steel welds caused more phase separation than the hyper duplex stainless steel weld.
- Processing history was more impactful on kinetics of 475°C-embrittlement than slight variations in composition.

## GRAPHICAL ABSTRACT

Fe and Cr phase separation in super (SDSS) and hyper (HDSS) duplex stainless steels

Level of Cr and Fe phase separation in ferrite  
5 min aging at 475 °C - Atom probe tomography



## ARTICLE INFO

### Article history:

Received 28 July 2021

Revised 16 August 2021

Accepted 18 August 2021

Available online 19 August 2021

### Keywords:

Spinodal decomposition  
Duplex stainless steels  
Atom probe tomography  
Welding, hot rolling  
475°C-embrittlement

## ABSTRACT

Fe and Cr phase separation in ferrite, causing 475 °C-embrittlement, was studied after very short aging times in super duplex stainless steel (SDSS) and hyper duplex stainless steel (HDSS) plates and welds. Atom probe tomography showed that hot-rolled SDSS, experiencing significant metal working, had faster kinetics of phase separations compared to the SDSS and HDSS welds after 5 min aging at 475 °C. The surface of the 33-mm SDSS plate had faster Fe and Cr phase separation and larger toughness drop. A higher density of dislocations next to the austenite phase boundary in ferrite, detected by electron channeling contrast, can promote the phase separation at the surface of the plate with lower austenite spacing. The toughness dropped in HDSS welds after aging, but SDSS welds maintained their toughness. An inverse simulation method considering an initial sinusoidal nanometric Cr and Fe fluctuation showed that Ni increases the interdiffusion of Cr in the system, resulting a higher degree of phase separation in SDSS welds than the HDSS weld. Within the composition range of the studied SDSS and HDSS materials, the processing influences the Fe and Cr phase separation more than the variation in composition during short aging or typical fabrication times.

© 2021 Published by Elsevier Ltd. This is an open access article under the CC BY-NC-ND license (<http://creativecommons.org/licenses/by-nc-nd/4.0/>).

\* Corresponding author at: Department of Engineering Science, University West, SE-461 86 Trollhättan, Sweden  
E-mail address: [Vahid.hosseini@hv.se](mailto:Vahid.hosseini@hv.se) (V. A Hosseini).

## 1. Introduction

Stainless steels, containing more than 12% Cr, have a self-healing cohesive chromium oxide passive layer, protecting them from corrosion. In ferritic, duplex (ferritic-austenitic), and martensitic stainless steels, Cr and Fe tend to separate during holding at intermediate temperatures, known as 475 °C-embrittlement [1,2]. It happens due to the presence of a miscibility gap in the Fe-Cr alloying system, and the decomposition is faster for higher Cr contents (<50% Cr) [3–7]. Although there are still some knowledge gaps regarding the kinetics of this separation, research has shown a dependence on the composition, microstructure, and processing history of the material.

It is known that Ni accelerates the kinetics of Cr and Fe separation both in ternary and industrially produced alloys [8,9]. Interestingly, compared to binary Fe-Cr alloy, ternary Fe-Cr-Ni alloys, with a higher degree of Fe-Cr separation, showed a much lower drop in impact energy values at the same aging time [8]. In one of the recent modelling studies, in contrast, it has been claimed that Ni retards the spinodal decomposition both thermodynamically and kinetically, which is conflicting with experiments [10]. The impact of Mo on spinodal decomposition is controversial in duplex stainless steels (DSS). Some studies [11–13] showed that Mo accelerates the kinetics of spinodal decomposition. In contrast, other studies [14,15] reported that it has no significant impact on the kinetics of Cr and Fe separation.

The microstructure may also impact the kinetics of Fe-Cr separation. Miller et al. [16] compared Fe-45 %Cr binary alloy with commercially produced duplex structure with ferrite composition of Fe-27.9at%Cr-4.8 %Ni-1.2 %Si-0.3 %Mn-0.15 %Mo. They interestingly showed that the phase separation is significantly faster in the commercially produced one with less Cr. Although the reason remained unanswered, the interdiffusion of alloying elements and the presence of austenite were considered as possible reasons. The presence of austenite significantly increases the kinetics of spinodal decomposition, but its reason is still not clear [9,17].

The impact of the processing is also more complex; as normally when the process changed, the chemical composition was also altered in different studies. Based on this, weld metal in DSS are normally considered more prone to spinodal decomposition, but they are normally over alloyed with Ni [18]. In other studies [19], it has been mentioned that applied stress during aging can significantly accelerate spinodal decomposition. The internal stresses coming from welding, therefore, were considered to attribute to the faster kinetics of phase separation compared to physically simulated high temperature heat affected zones [19].

The recent introduction of highly alloyed DSS, such as super duplex stainless steels (SDSS) and hyper duplex stainless steels (HDSS), has brought faster kinetics of high temperature phase transformations, such as the formation of sigma, chi, and R-phase

[20–26]. Spinodal decomposition is faster in the SDSS compared to standard and lean DSS grades, but not studied in HDSS. Time-temperature-toughness diagrams show that the toughness drops with up to 50% already after 3 min heat treatment of SDSS at 475 °C [27]. In a recent study, it was shown that Fe and Cr separated in ferrite phase of as-fabricated thick SDSS hot-rolled and hot isostatic processed materials [28]. Keplinger et al. [29] also reported that HDSS forged products had an unexpected low toughness of 30 J at –46 °C compared to a toughness of 300 J at –46 °C in SDSS samples, without any indication of secondary phases. This could be an indication of possible Fe and Cr phase separation during the fabrication of HDSS. During the application, 475 °C-embrittlement is the most important barrier to use SDSS at intermediate temperatures. Cojocar et al. [30] reported a significant toughness loss after 3 h aging of type-2507 SDSS plate at 400 °C. Pettersson et al. [31] also stated that Fe and Cr phase separation, toughness loss, and hardness increase after 3000 h aging of type-2507 SDSS plate at 300 °C. Therefore, Fe and Cr phase separation and 475 °C-embrittlement can degrade SDSS and HDSS during fabrication and application even during a short heating time to the temperature range of 300–500 °C. However, further study is needed to investigate the relationship between Fe and Cr phase separation and resulting 475 °C-embrittlement for short aging time in SDSS and HDSS.

In addition to the specific knowledge gap for HDSS and SDSS, the general understanding regarding the impact of fabrication, processing, microstructure, and composition on the kinetics of spinodal decomposition was not satisfactorily addressed. This study, therefore, aims at comparing the kinetics of Fe and Cr phase separation after a short heat treatment of 5 min at 475 °C for SDSS and HDSS welds and hot-rolled plates. The aged samples, produced by Gleeble physical simulator, were studied using atom probe tomography (APT), electron backscattered diffraction (EBSD), electron channeling contrast imaging (ECCI), kinetics simulation, and microhardness and impact toughness testing. The study adds new insight into the effect of processing parameters and chemical composition on the kinetics of Fe and Cr separation and the concomitant 475 °C-embrittlement.

## 2. Experiments

### 2.1. Materials

The chemical composition of samples produced from welds and the hot-rolled plate is detailed in Table 1. To produce the weld samples, a V-shape groove was filled using gas metal arc welding with SDSS filler without tungsten (SWeld) and with tungsten (SWWeld), and gas tungsten arc welding with HDSS filler metal (HWeld).

**Table 1**  
Chemical composition of as-fabricated samples (wt%) with Fe as balance.

Sample desc.		SWeld	SWWeld	HWeld	PlateS	PlateC
C	Comb.	0.01	0.01	0.01	0.02	0.02
Si	OES	0.4	0.4	0.3	0.3	0.3
Mn	XRF	0.8	0.4	0.9	0.7	0.7
P	OES	0.02	0.02	0.02	0.03	0.02
S	Comb.	0.0005	0.0007	0.0005	0.0005	0.0005
Cr	XRF	25.6	25.1	26.5	25.0	25.0
Ni	XRF	9.4	9.3	6.5	7.1	7.1
Mo	OES	3.8	3.9	4.7	3.9	3.9
W	OES	0.64	0.002	0.002	0.05	0.06
Co	OES	0.07	0.04	0.6	0.1	0.1
N	Fusion	0.33	0.26	0.38	0.28	0.29
O	Fusion	0.01	0.004	0.007	0.003	0.003

The plate samples were extracted from a 33-mm thick SDSS plate from its center (PlateC) and surface region (PlateS). For the hot-rolling, the plate was casted with a thickness of 140 mm and rolled to a final thickness of 33 mm with 10 passes from the starting of 1229 °C to the final temperature of 1148 °C.

## 2.2. Gleeble physical simulation

Samples with the size of 55 mm × 10 mm × 6 mm were produced to study the kinetics of phase separation. The heat treatment was performed using a Gleeble 3800 physical simulator, where a combination of ohmic heating and argon quenching produced the programmed cycles. A thermocouple was attached at the center of each sample, controlling the thermal cycles. All samples for characterization were produced from the location of the thermocouple and notches for Charpy impact toughness test were also placed in the same location. The details of heat treatment cycles and sample designations are shown in Table 2.

## 2.3. Characterization and mechanical testing

### 2.3.1. Optical microscopy

The samples were ground and polished using a standard preparation procedure and directly etched with the modified Beraha reagent for 10 s. The cross section of the sample was investigated using Zeiss Axio Imager.M2m optical microscope. To measure the ferrite content for each sample, at least five different micrographs at 200X magnification were evaluated with ImagePro software. To reveal the possible presence of secondary phases, the area close to the fractured surface of PlateS-TC1-475 and PlateC-TC1 tested samples were electrolytically etched with oxalic acid.

### 2.3.2. Scanning electron microscopy

PlateS and PlateC samples were studied with a ZEISS Gemini scanning electron microscopy (SEM) 450 equipped with an Oxford Instruments Symmetry S2 electron backscattered diffraction (EBSD) detector. To eliminate any stress and the strain induced during the sample preparation, after grinding with 2500 grade SiC paper, the samples were electropolished using 150 g citric acid, 300 g distilled water, 600 ml H<sub>3</sub>PO<sub>4</sub>, and 450 ml H<sub>2</sub>SO<sub>4</sub> for 25 s at 15 V. A step size of 0.4 μm, a spot size of 1 nm, a voltage of 15 V and a working distance of 12 mm were used to perform EBSD. Band contrast data was extracted to verify the quality of the acquired

**Table 2**  
Designation of investigated samples.

Designation of initial samples	
PlateC	Sample cut from the center of 33 mm super duplex stainless steel plate-cooling time between 500 and 400 °C about 20 s
PlateS	Sample cut from the surface of 33 mm super duplex stainless steel plate cooling rate between 500 and 400 °C about 2 s
SWeld	Super duplex stainless steel weld metal
SWWeld	Tungsten containing super duplex stainless steel weld metal
HWeld	Hyper duplex stainless steel weld metal
Designation of heat treatments	
TC1	Thermal cycle 1: Heat treatment at 1100 °C for 3 min, 20 s cooled down to 1000 °C, and quenching to below 300 °C followed by natural cooling
TC2	Thermal cycle 2: Heat treatment at 1100 °C for 3 min, 20 s cooled down to 1000 °C, and quenching to below 550 °C, 40 s to 400 °C followed by natural cooling
475	5 min at 475 °C followed by natural cooling
1150	3 min at 1150 °C-20 s to 1030 °C, quenching to below 300 °C (followed by natural cooling if not aged)
All studied	samples based on the above designations
Plate	PlateS, PlateC, PlateS-TC1-475, PlateC-TC2-475, PlateC-TC1
Welds	SWeld-1150, HWelds-1150, SWWeld-1150, SWeld-1150-475, HWelds-1150-475, SWWeld-1150-475

images. Then, phase and inverse pole figure (IPF) maps for each sample were extracted. To measure the strain in the sample, local average misorientation and Kernel misorientation were calculated. The geometrically necessary dislocation density was also measured using a Kernel misorientation approach [32]. The mean angular deviation (MAD) or pattern misfit, showing how much measured and simulated Kikuchi patterns fit with each other [33], were also visualized for each condition. The EBSD data analyses were performed with AZtec crystal software (Oxford Instruments).

In order to analyze the dislocations in the plate samples, ECCI was performed using a voltage of 30 kV, a current of 10nA, a working distance of 8 mm, a tilt of 2°, using outer diodes of a backscattered electron (BSE) detector in medium intensity mode. A high image resolution with low capturing speed was performed to take high quality images, otherwise, it was not possible to image the dislocations. Only a few ferrite grains were in the right direction, satisfying the crystallographic orientation, for imaging the dislocations.

### 2.3.3. Atom probe tomography

Atom probe tomography was employed to study the level of phase separation. To prepare the specimens, 0.3 × 0.3 × 15 mm<sup>3</sup> rods were cut. Each rod was placed in an aluminum holder and electropolished in 10% perchloric acid at 19 V until a thin neck had formed. This was followed by electropolishing in 2% perchloric acid at 19 V until the rod separated at the position of the neck, giving two needle-shaped specimens. A local electrode atom probe, LEAP 3000X HR, equipped with a reflectron was employed. The analysis was performed at a temperature of 55 K with a voltage pulse fraction of 20%, a pulse frequency of 200 kHz, and an evaporation rate of 0.2%. The APT data reconstruction was performed using IVAS 3.4/3.6, with a field of 33 V/nm, a geometric field factor (k) of 4.0, and an image compression factor of 1.65. Radial distribution functions (RDFs) were used to analyze the extent of the spinodal decomposition, whereby the radial concentration profile from each and every detected Cr atom was calculated and averaged. In this study, a step size of 0.1 nm was selected and the Cr concentration was normalized based on the measured concentration. More details about this method can be found in Ref. [3].

### 2.3.4. Mechanical testing

The microhardness of the ferrite was measured using Shimadzu HMV-2 with a force of 0.01 N and the average of 10 measurements was reported. The impact test was performed on sub-sized samples, produced using Gleeble physical simulator. The notch was placed where the thermocouple was located at the center of each sample, or plate, both TD and ND surfaces were measured. The Charpy impact toughness test was performed out at - 40 °C using a Zwick Roll machine with a sample size of 55 mm × 10 mm × 5 mm. Three samples were tested for each condition, except for the HDSS weld (two tested samples).

## 2.4. Thermodynamic calculations

Equilibrium calculations were performed to predict the nitrogen content of the ferrite phase at the solution annealing temperature using the Thermo-Calc software, with the TCFE9 database. Diffusion simulations were performed using Dictra and TCFE9 and MOBF5 databases to study the interdiffusion of Cr with and without the presence of Ni. As the Dictra software does not model spinodal decomposition, an inverse technique was applied. In this approach, homogenization of a pre-existing sinusoidal Cr and Fe composition profile was simulated at 475 °C for 5 min. The initial maximum and minimum Cr content was selected as 31 wt% and 29 wt%, respectively. Then, the homogenization simulation was performed for heat treatment of Fe-30 at.% Cr and Fe-30 at. Cr-2

at.% Ni. The difference between the maximum and minimum Cr content may indicate the kinetics of Cr interdiffusion in each system.

### 3. Experimental results

#### 3.1. Microstructure and mechanical properties

The microstructure of the samples in their initial condition and after different heat treatments was shown in Fig. 1. As may be seen, the plate samples have elongated austenite grains in the rolling direction, while the all-weld metal samples have a typical solidification microstructure, containing grain boundaries, Widmanstätten, and intragranular austenite. In the plate, the microstructure is finer close to the surface with shorter austenite spacing, while it has a slightly coarser microstructure with Widmanstätten-like austenite in the center. Typical austenite spacing is  $11 \pm 6 \mu\text{m}$  close to the surface and  $16 \pm 10 \mu\text{m}$  in the center. The solutionized all-weld metal samples did not have any secondary austenite clusters or secondary phases.

The ferrite fraction of samples after their respective heat treatment is shown in Fig. 1. The lowest ferrite fraction in the plate samples is for PlateC, while it is almost similar in the others. For the welds, the HDSS-1150-475 shows the highest value of 56% ferrite, while SWWeld-1150-475 had only 38% ferrite.

The microhardness of the ferrite and the impact toughness energies for the investigated samples are shown in Fig. 2. Aging for 5 min at 475 °C increased the microhardness of the ferrite in all samples, where the most significant ones were the plate samples with about 90–125 HV0.01 increase. The welds, however, had an increase of only 20–30 HV0.01. The same trend was also observed in the toughness values, where the most significant drop was seen for the plate samples. The PlateS was the most affected one with a 72 J reduction in toughness. SWWeld and SWeld interestingly maintained their toughness after aging, but HWeld toughness slightly dropped from 97 J to 85 J.

The microstructure of solution-annealed (TC1) and solution-annealed-aged (TC1-475) plate samples close the fracture area is shown in Fig. 3. Nitride clusters (the black etched areas) were found in ferrite before and after aging. The toughness of the solution annealed sample (with nitrides) was in the same range as that in as-received plate samples (without nitrides).

#### 3.2. Atom probe tomography

The chemical composition of ferrite obtained by APT is shown in Table 3. The plate samples have quite same chemical composition with some variation in Cr, Ni, and Mo, which is expected from APT results. HWeld-1150-475 has a composition very close to the chemical composition of SWeld-1150-475, except for lower Ni and higher Co contents.

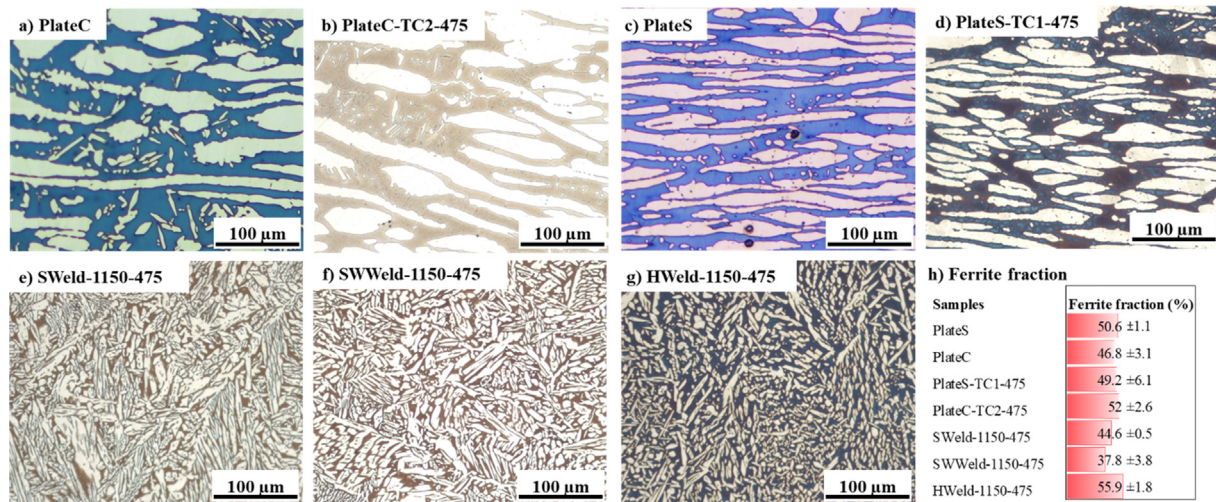


Fig. 1. Microstructure and ferrite fraction of the investigated samples. The plate samples have elongated grains in the rolling directions. The welds show grain boundaries, Widmanstätten, and intragranular austenite.

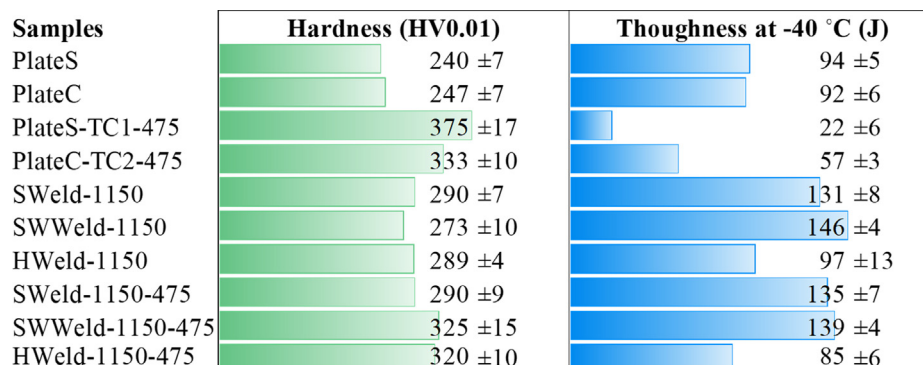
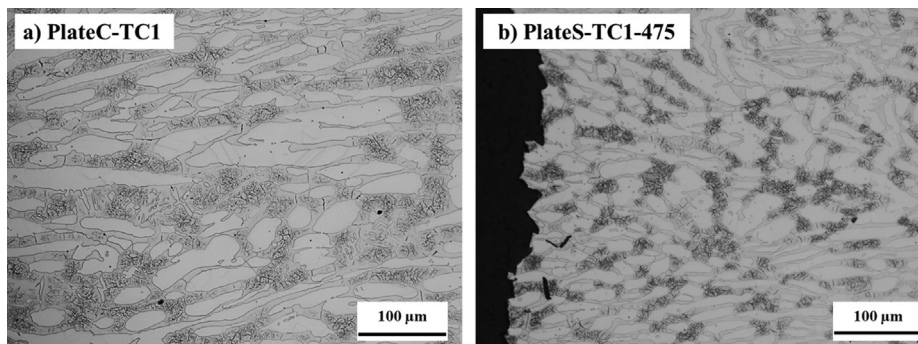


Fig. 2. Ferrite fraction, microhardness of ferrite, and toughness at -40 °C.



**Fig. 3.** a) Microstructure of the solution annealed plate sample (PlateC-TC1) with a toughness of 96 kJ b) Microstructure of solution-annealed-aged plate sample (PlateS-TC1-475) with a toughness of 25 kJ. Nitrides are present before and after aging in the plate samples.

**Table 3**  
Chemical composition of ferrite studied with APT.

at%	PlateS	PlateC	PlateS-TC1-475	PlateC-TC2-475	HWeld-1150-475	SWeld-1150-475	SWWeld-1150-475
Si	0.9	0.9	0.8	0.8	0.73	1	1.01
Cu	0.1	0.1	0.1	0.12	0.13	0.08	0.3
Cr	28.0	27.8	26.6	27.7	27.8	27.9	27.5
Mn	0.6	0.6	0.7	0.6	0.9	0.3	0.7
Ni	4.5	4.4	5.7	5.1	5.9	7.3	7.3
W	0.07	0.8	0.04	0.02	0.02	0.03	0.15
Mo	3.2	3.4	2.7	2.6	3.2	3.1	2.8
Co	0.11	0.11	0.12	0.11	0.84	0.03	0.08
Fe + minor elements	Bal.	Bal.	Bal.	Bal.	Bal.	Bal.	Bal.

The normalized Cr-Cr RDFs of the APT studied samples for the plate and weld samples are shown in Fig. 4. The plate samples showed significant increases of their Cr-Cr RDF values for small

distances, indicating decomposition, after 5 min heat treatment, which is more pronounced for the PlateS. The welds did not show significant Cr and Fe separations compared to the plate, but the ranking indicated that the highest normalized Cr concentration is for SWeld-1150-475, followed by SWWeld-1150-475 and HWeld-1150-475. The normalized Cr-Cr RDF of austenite for a plate sample is shown in the diagram to indicate the behavior for a random distribution of Cr and Fe in a phase, i.e. the curve is close to unity also for small distances.

As the separation was relatively well-developed in the PlateS-TC1-475 and PlateC-TC2-475, the spinodal decomposition is visible by isoconcentration surfaces, as shown in Fig. 5a. For the other samples, this method gave less clear results.

### 3.3. Electron backscatter diffraction

To investigate the difference between PlateC and PlateS, EBSD was performed. Band contrast images of the two studied samples are shown in Fig. 6. Both samples show sharp and clear images and no indications of scratches or deformed surfaces were observed.

The EBSD phase and grain orientation maps of the plate samples are shown in Fig. 7. No significant differences were found between these two samples at this magnification from the view of phase fraction and grain orientation, despite that the ferrite is slightly finer in PlateS. Some Widmanstätten-like austenite were observed in the PlateC sample with the same orientation as their main austenite grains.

The local average and Kernel misorientations and geometrically necessary dislocation (GND) density of the ferrite for PlateC and PlateS are shown in Fig. 8. As may be seen, the ferrite in PlateS shows higher misorientation. The GND density is also higher in PlateS. The values are varying with the location in each condition, which means that some grains in PlateC may have locally higher values than those in PlateS.

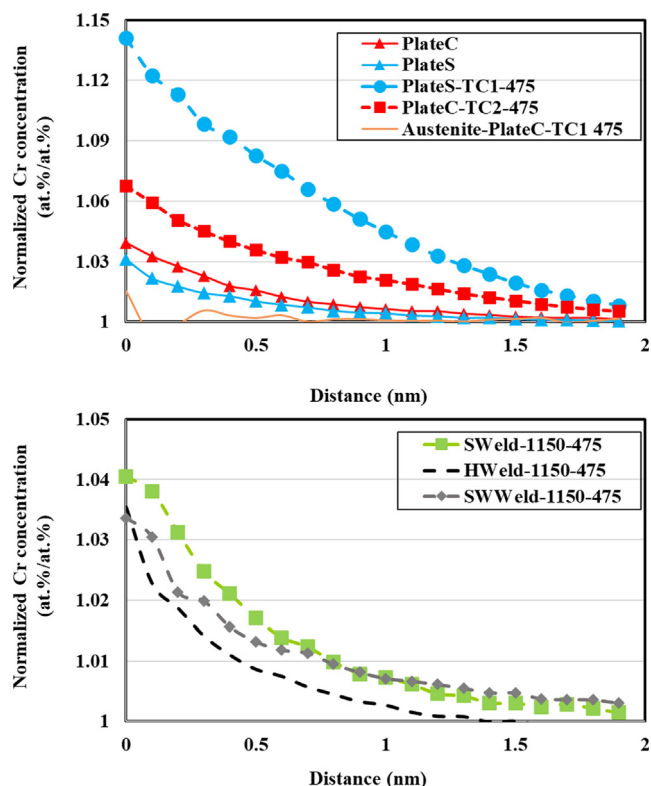


**Fig. 4.** Normalized Cr-Cr RDFs in plate and weld samples (note the different ordinate scaling).

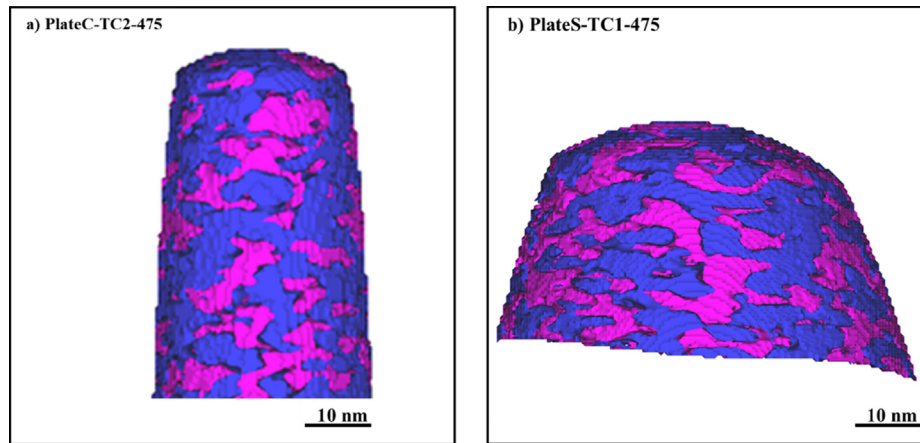


Fig. 5. Spinodal decomposition in PlateS-TC1-475 with Fe 62 at.% and Cr 27 at.% isoconcentration surfaces.

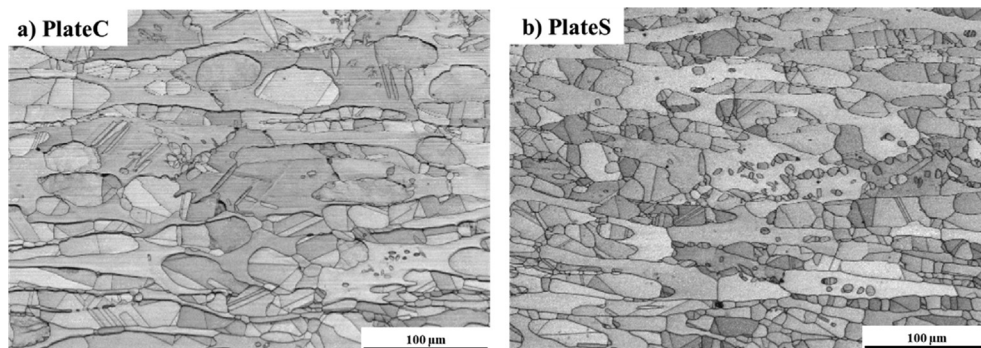


Fig. 6. Band contrast images of two plate samples, showing a high quality indicating a successful electropolishing procedure.

The other approach to study lattice defects using EBSD data is mean angular deviation (MAD) maps, showing the misfit between calculated and simulated Kikuchi patterns for each point [34,35], as illustrated in Fig. 9. As may be seen, PlateS has higher values compared to PlateC. It should be noted that the MAD is not uniform in the samples.

### 3.4. Electron channeling contrast imaging

The ECCI micrographs of as-received plate samples are shown in Fig. 10. Only a few ferrite grains in both samples were in the direction where the observation of dislocations was possible. In both samples, the location close to the austenite had higher dislocation density, which is more visible in PlateS. The dislocation density is seemingly higher in the PlateS.

## 4. Interdiffusion simulation

In this study, we developed an inverse model to solely study Cr interdiffusion during spinodal decomposition with and without the presence of Ni. Since Dictra cannot model the Fe and Cr separations via the spinodal decomposition, we introduced a Cr fluctuation and then run homogenization at 475 °C for 5 min, as described in the experimental section. For the same Cr fluctuation, we also added 2 at.% Ni. The illustration of this calculation for the Fe-Cr system is shown in Fig. 11. As may be seen, the maximum and minimum contents of Cr get closer together with the presence of Ni.

## 5. Discussion

### 5.1. Kinetics of the Fe-Cr phase separation

The normalized Cr-Cr RDFs in all studied samples, together with values from literature, are shown in Fig. 12. The literature data is for the same material, but heat treated at lower temperatures. It should be noted that the chemical compositions of the ferrite phase in these materials [19,36] were very close to the ferrite composition of the plate samples. Zhou et al. [19] produced the simulated high temperature heat affected zone by heat treating 2507 SDSS plate to 1350 °C, air cooling to 1050 °C and quenching, followed by aging at 325 °C for 5,800 h. Pettersson et al. [36], in contrast, studied the as-fabricated plate (hot rolled) after aging at 300 °C for 3,000 h. As may be seen, 5 min aging of plate samples in this study has a much more significant influence on the Cr and Fe separation compared to the long aging time in the other studies. However, for the welds, the numbers are closer to the literature data.

#### 5.1.1. Hot-rolling

Despite the similar composition of the heat-treated plates, PlateS-TC1-475 showed more development of spinodal decomposition than that for PlateC-TC2-475, as shown in Fig. 4. The purpose of the TC1 and TC2 heat treatments was to remove any possible intermetallics and local segregations in PlateC and PlateS but, at the same time, produce materials close to the initial state from the view of the cooling condition. Since the chemical compositions

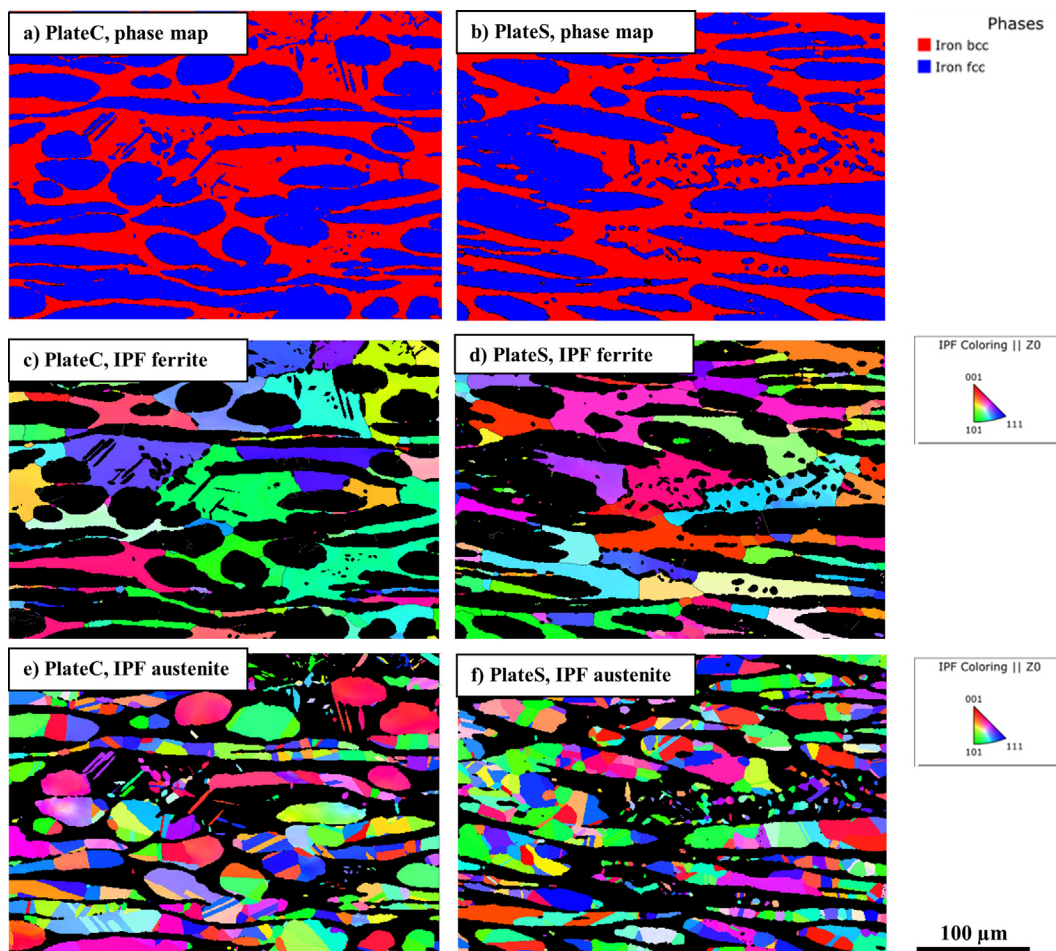


Fig. 7. Phase maps and IPF of ferrite and austenite in PlateC and PlateS.

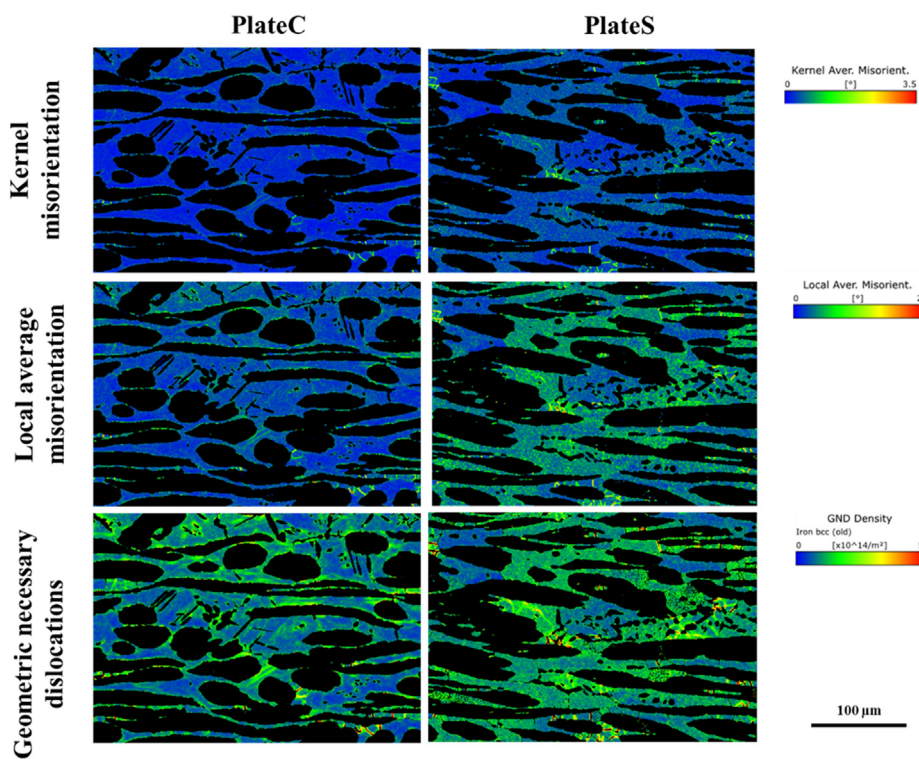


Fig. 8. Kernel and local average misorientation and GND density of ferrite in PlateC and PlateS.

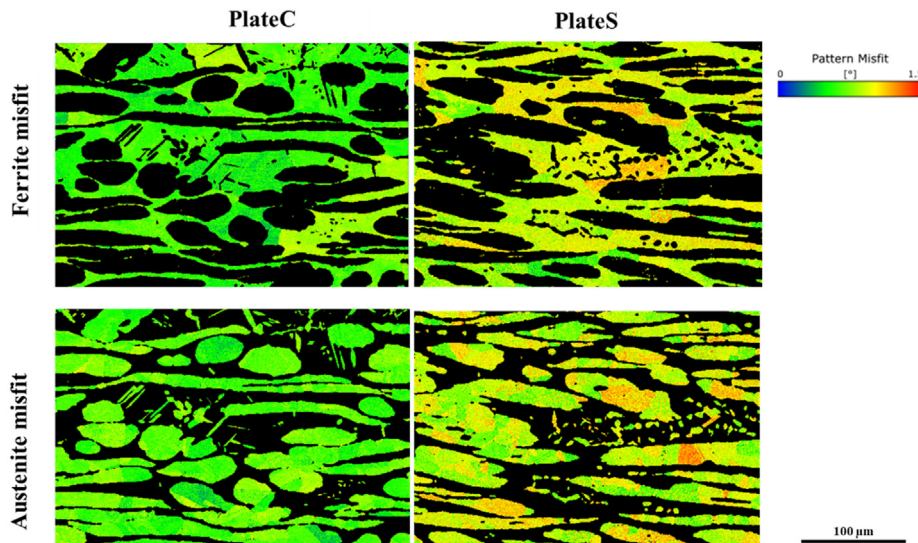


Fig. 9. MAD maps of ferrite and austenite, which is higher in PlatesS.

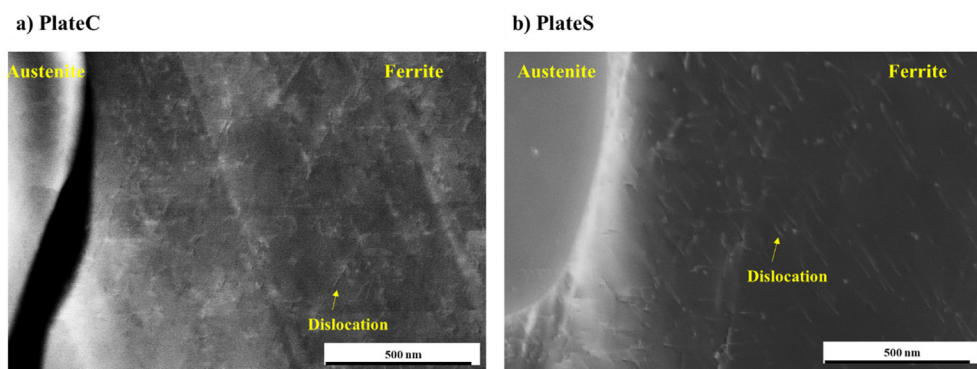


Fig. 10. Electron channeling contrast imaging of ferrite/austenite phase boundary in a) PlateC and b) PlateS. Both samples show some dislocations, where the location closer to the phase boundary shows higher dislocation number density.

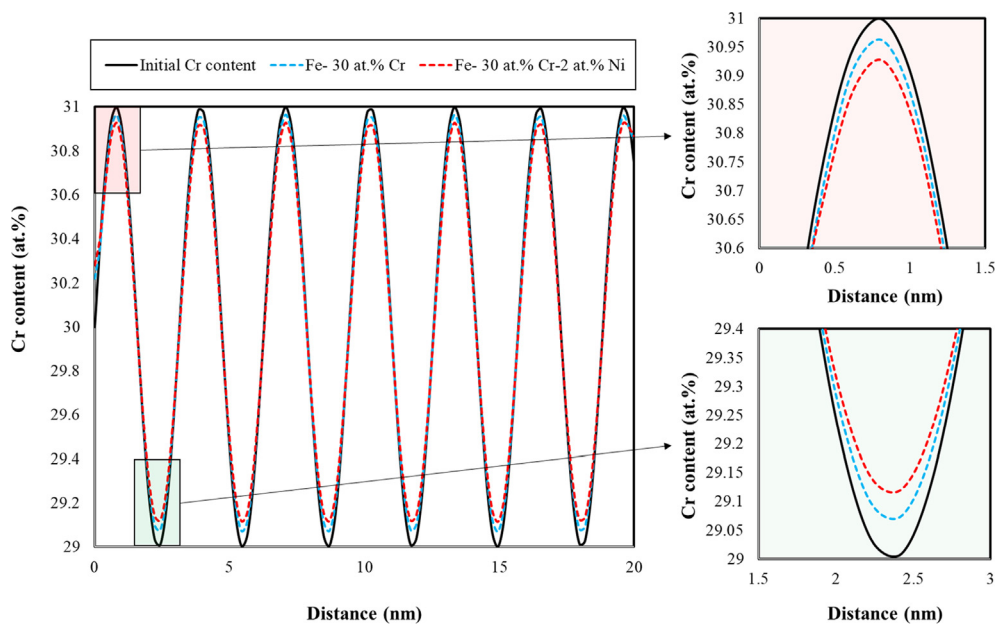


Fig. 11. Sinusoidal fluctuation of Cr at time 0 s and 300 s for Fe – 30 at.% and Fe- 30 at.% – 2 at.% Ni. The Ni-containing composition shows faster homogenization.

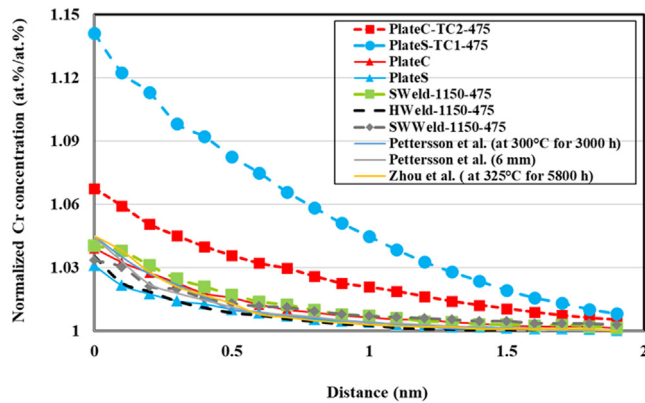


Fig. 12. Comparison of normalized Cr-Cr RDFs in this study compared to literature data.

in plate samples are quite similar (Table 3), therefore, the discussion regarding their difference in Fe and Cr phase separation kinetics can be directed toward their processing condition.

The processing condition can mainly impact the ferrite stability and the interdiffusion coefficient of different elements. The processing history of PlateC and PlateS have some differences that can influence the kinetics of the Fe and Cr separation:

**Level of stress/strain:** The highest shear stress during hot rolling occurs in the surface, resulting in finer austenite spacing in PlateS [37,38], while PlateC still poses the solidified microstructure with Widmanstätten austenite (Fig. 1 and Fig. 7). The reason is that the surface is in contact with the rollers and high shear stress and more equivalent strains develop during rolling, whereas in the center the material can be displaced with lower deformation and stress.

**Cooling condition:** Slow cooling between 550 and 400 °C allowed the ferrite and austenite to accommodate the stresses caused by hot rolling and by the differences in thermal expansion coefficients during cooling. In addition, slower cooling may help to equilibrate the vacancies formed during hot rolling and/or high temperature annealing.

These processing conditions result in higher values for local average and Kernel misorientations, GND density, MAD, and perhaps the density of mobile dislocations in PlateS compared to PlateC, indicating a higher level of stresses during rolling and more lattice defects (Fig. 8 and Fig. 9). First principle simulations showed that strain can decrease the stability of ferrite, even for diluted compositions [39]. The presence of lattice defects such as vacancies and dislocations can also promote spinodal decomposition [40–44]. Particularly, as shown in ECCI micrographs (Fig. 10), the dislocation density in the ferrite is higher closer to austenite grains. Therefore, more austenite/ferrite phase boundaries can increase the number of dislocations. The ECCI observation is in good agreement with Johansson et al. [44], where they predicted a higher level of stresses closer to the austenite boundary in ferrite by finite element simulation of a duplex structure during rolling. Xu et al. [45] reported that a higher solutionizing temperature of binary Fe-53 at.% Cr resulted in faster spinodal decomposition due to the higher content of quench-in vacancies. The result of this model alloy fits very well with the results in this study, where slow cooling between 550 and 400 °C resulted in lower development of phase separation during the subsequent aging.

### 5.1.2. Welds

HWeld-1150–475 had slower kinetics of phase separation than SWeld-1150–475 and SWWeld-1150–475 (Fig. 4). The main differences between HWeld-1150–475 and SWeld-1150–475 were 1.5

at.% higher Ni in HWeld-1150–475 and the presence of Co in HWeld-1150–475 (Table 3). Based on the literature, Co can increase the kinetics of spinodal decomposition, therefore, it could not be the reason for slower Cr and Fe separation in HWeld [46]. The different Ni contents, therefore, explain why the kinetics is faster in SWeld-1150–475 despite a slightly higher Co content in HWeld. Based on the first principle calculations performed by Ponomareva et al. [39], the addition of Ni decreases the stability of ferrite, which fits well with our results. The inverse modelling (Fig. 11) also showed that the presence of Ni facilitates the interdiffusion of Cr in the system. The lower ferrite stability and the faster interdiffusion of Cr in the presence of Ni, therefore, result in more Cr and Fe separation in SWeld-1150–475 compared to HWeld-1150–475.

The Cr-Cr RDF curve of SWWeld-1150–475 is located between the curves of HWeld-1150–475 and SWeld-1150–475 (Fig. 4). Seemingly, this could be the result of higher Cu and W content in SWWeld-1150–475. It has already been stated that Cu might reduce the kinetics of the Fe and Cr phase separation [28,47]. However, the other elements, such as Mn and Mo, had some minor differences between SWeld-1150–475 and SWWeld-1150–475, which may impact the kinetics of the phase separation. Although the most recent study showed that Mn and Mo do not have any significant effects on the kinetics of Fe and Cr separations [48], further systematic studies are needed to draw a solid conclusion on the influence of W and Cu on the kinetics of Fe and Cr phase separation. In addition to the substitutional alloying elements, ThermoCalc calculations reveal that the equilibrium contents of nitrogen in ferrite are 0.32 at.% for SWeld, 0.33 at.% for SWWeld, and 0.42 at.% for HWeld at 1150 °C. Nitrogen can change not only the partitioning of alloying elements in ferrite and austenite [49], also the kinetics of phase transformations [50]. In a recent study, Zhang et al. [50] reported that raising nitrogen content reduces the precipitation kinetics of sigma phase but accelerates nitrides formation due to the change in the Cr, Mo, N diffusion rates and activities in HDSS hot-rolled plate. Bliznuk et al. [51], however, predicted that nitrogen addition cannot be effective to prevent Cr and Fe phase separation during aging at 475 °C, but no aging was performed to justify it. A more systematic study is, therefore, needed to investigate the influence of nitrogen on the kinetics of spinodal decomposition.

### 5.1.3. Comparison of hot-rolling and welding

PlateS-TC1-475 indicates that despite higher contents of Cr and Ni in SWeld (Table 3), the kinetics of spinodal decomposition is much slower in the solution annealed welded samples (Fig. 12). Therefore, the weld microstructure, by itself, seems to reduce the phase separation kinetics if annealed. This is in contrast with findings in other studies, where it was observed that welding will increase the kinetics of Fe-Cr separation. Zhou et al. [19] reported that weld metal has faster kinetics than the plate, while in that study they heat treated the base metal to 1350 °C followed by slow cooling to 1050 °C, which changed the hot-rolled elongated grains to equiaxed ones. In contrast, their weld metal was cut from as-fabricated all weld metal structure. Garfinkel et al. [52] also reported that their weld had faster kinetics of spinodal decomposition after a long aging time (1,000 h) at 427 °C, while their weld had 3% higher Ni than the base metal and no information regarding the ferrite composition was available. In addition, it should be noted that our study is expected to be more affected by processing, since, during the longer aging time, possible stress relief of a component can change the kinetics of phase separations. In contrast, during short aging times, which is valid for the fabrication steps, level of internal lattice defects, and strain are expected to play a more crucial role for the kinetics of phase separation. For instance, it was stated that the presence of vacancies is more prominent for

making the kinetics of spinodal decomposition faster at the initial stage of phase separation [45].

The welds, with as-solidified structure and non-deformed ferrite and austenite, are expected to have a low level of lattice defects (such as stacking fault, dislocations, and vacancies). In contrast, during the plate production, the thickness of the 140-mm-thick casted slab was reduced to 33 mm by 10 passes of hot-rolling. The presence of high dislocation density and the formation of subgrains in ferrite [53,54] and dislocation pile-up in ferrite/austenite were observed in hot-deformed samples (this study). So, more deformation, lattice defects, and subgrains facilitated the phases separation. This is in good agreement with the difference of Fe and Cr phase separation between the plate center and surface, where the results showed that plate center with microstructure closer to as solidified condition (less deformed) has slower kinetics of phase separation. More fundamental studies are needed to explain the faster kinetics in hot rolled plates than that in the welds, particularly by assessing the lattice defects and residual stresses during hot deformation steps.

## 5.2. 475 °C -Embrittlement

In general, the drop in toughness of welds after the short aging time was not as dramatic as for the plate samples, fitting well with their low degree of Fe and Cr separation (Fig. 2). PlateC-TC2-475 with a lower Cr-Cr RDF had higher toughness compared to PlateS-TC1-475. Therefore, the level of phase separation, microhardness, and impact toughness fit very well for the plate samples (Fig. 2). In addition to the level of phase separation, possibly nonuniform phase separation close to the austenite boundaries and grain to grain variations of the phase separation, can facilitate the crack growth in PlateS-TC1-475.

Nitrides formed in the plate during cooling after solution annealing, since rapid cooling caused the supersaturation of nitrogen in ferrite, followed by nitrides precipitation at lower temperatures [55]. As the same distribution of nitrides was present before and after aging in the plate samples, the drop in toughness after aging cannot be directly related to the presence of nitrides. Pettersson et al. [56] also did not find any significant reduction of impact toughness in nitrides-containing DSS. However, the presence of nitrides in more brittle ferrite with a high Fe and Cr separation level synergized the embrittlement in the aged condition. In contrast, in the solution-annealed sample, the presence of nitrides in less brittle ferrite with a low Fe and Cr separation level was not so detrimental for toughness.

In the welds, the lower impact toughness of HWeld-1150 is the result of a higher ferrite fraction and lower Ni content than those for other solutionized welds before aging (Fig. 2). SWeld-1150-475 and SWWeld-1150-475 maintained their toughness even with increases in the microhardness of the ferrite after aging. In contrast, HWeld-1150, with the same level of microhardness increase as the SDSS welds after aging, showed a 12 J drop in the toughness. The main differences between SDSS and HDSS welds are 2 at.% higher Ni content in the ferrite, a larger austenite fraction in the SDSS welds, and a higher level of nitrogen content in the HWeld. Despite that Ni increases the kinetics of Cr and Fe separation, it helps the ferrite to maintain its impact toughness after the phase separation during short aging times. This was also seen in Fe-Cr and Fe-Cr-Ni model alloys, where, with much degree of phase separation in Fe-Cr-Ni, the drop in toughness was much more noticeable in Fe-Cr [57]. In addition, a higher austenite fraction can help to decrease the interconnection among ferrite grains and hinder the cracks to grow. Golovin et al. [58] reported that the high N in HWeld could pin the dislocations at the initial stage of aging, which may result in the reduction of toughness in HWeld-1150-475.

To sum up, toughness is affected not only by the level and inhomogeneity of nanostructured phase separation but also by the morphology, composition, and fraction of different phases as discussed for the welded samples. To understand the effect of composition on the kinetics of 475 °C-embrittlement, it is of prime importance to compare all factors including processing, microstructure, nanostructured features, residual stresses, hardness, and toughness.

## 6. Conclusions

Cr and Fe phase separation was studied after very short aging times at 475 °C in solution annealed SDSS and HDSS hot-rolled plates and welds using APT, EBSD, interdiffusion simulation, and microhardness and impact toughness testing. The hot-rolled plates had more Fe and Cr separation, higher ferrite microhardness increase, and larger drop in the impact toughness energies compared to the welds after 5 min aging. The surface of the plate (cooled faster) had more developed phase separation and larger toughness drop compared to the center of the plate (cooled slower) after aging. EBSD showed a higher level of misorientation, density of geometrically necessary dislocations, and mean angular deviation in the surface of the plate compared to the center of the plate. ECCI also showed that more dislocations were present closer to the austenite boundary in the ferrite, which can promote Fe and Cr separation in PlateS. In welds, HDSS showed a lower level of Fe and Cr separation compared to SDSS; however, it had a larger drop in toughness. It was attributed to the higher content of Ni and higher austenite fraction in SDSS compared to HDSS. Interdiffusion simulation showed that Ni accelerates the diffusion of Cr in the Fe-Cr system. Finally, it can be concluded, for the studied composition, that the influence of processing is more crucial than the slight variation in composition. Therefore, the process parameters with a low level of residual stress/strain and more lattice defects in finished products are more favorable to avoid 475 °C-embrittlement during short aging and fabrication times.

## Declaration of Competing Interest

The authors declare that they have no known competing financial interests or personal relationships that could have appeared to influence the work reported in this paper.

## Acknowledgment

The APT was performed in Chalmers Materials Analysis Lab (CMAL). The author would like to acknowledge KK-Stiftelsen for funding of "ALWAYS project". Kjell Hurtig, from University West, Sweden, is acknowledged for his help in Gleeble simulation.

## References

- [1] J.-O. Nilsson, Super duplex stainless steels, *Mater. Sci. Technol.* 8 (8) (1992) 685–700.
- [2] J.-O. Nilsson, G. Chai, The physical metallurgy of duplex stainless steels, Duplex Stainless Steel Conference, Beaune, France, 2010.
- [3] J. Zhou, J. Odqvist, M. Thuvander, P. Hedström, Quantitative evaluation of spinodal decomposition in Fe-Cr by atom probe tomography and radial distribution function analysis, *Microsc. Microanal.* 19 (3) (2013) 665–675.
- [4] J. Zhou, J. Odqvist, A. Ruban, M. Thuvander, W. Xiong, J. Ågren, G.B. Olson, P. Hedström, Effect of solution treatment on spinodal decomposition during aging of an Fe-46.5 at.% Cr alloy, *J. Mater. Sci.* 52 (1) (2017) 326–335.
- [5] M. Hedin, J. Massoud, F. Danoix, Influence of the quenching rate on the spinodal decomposition in a duplex stainless steel, *Le Journal de Physique IV* 6 (C5) (1996) C5-235–C5-240.
- [6] J.C. LaSalle, L.H. Schwartz, Further studies of spinodal decomposition in Fe-Cr, *Acta Metall.* 34 (6) (1986) 989–1000.

- [7] M. Hörnqvist, M. Thuvander, A. Steuwer, S. King, J. Odqvist, P. Hedström, Early stages of spinodal decomposition in Fe–Cr resolved by in-situ small-angle neutron scattering, *Appl. Phys. Lett.* 106 (6) (2015) 061911, <https://doi.org/10.1063/1.4908250>.
- [8] H.D. Solomon, L.M. Levinson, Mössbauer effect study of '475 C embrittlement' of duplex and ferritic stainless steels, *Acta Metall.* 26 (3) (1978) 429–442.
- [9] J.E. Brown, G.D.W. Smith, Atom probe studies of spinodal processes in duplex stainless steels and single- and dual-phase Fe–Cr–Ni alloys, *Surf. Sci.* 246 (1–3) (1991) 285–291.
- [10] T. Barkar, Modelling phase separation in Fe–Cr alloys: A continuum approach, *KTH Royal Inst. Technol.* (2018).
- [11] J.D. Tucker, M.K. Miller, G.A. Young, Assessment of thermal embrittlement in duplex stainless steels 2003 and 2205 for nuclear power applications, *Acta Mater.* 87 (2015) 15–24.
- [12] C. Pareige, J. Emo, S. Saille, C. Domain, P. Pareige, Kinetics of G-phase precipitation and spinodal decomposition in very long aged ferrite of a Mo-free duplex stainless steel, *J. Nucl. Mater.* 465 (2015) 383–389.
- [13] T.G. Lach, A. Devaraj, K.J. Leonard, T.S. Byun, Co-dependent microstructural evolution pathways in metastable  $\delta$ -ferrite in cast austenitic stainless steels during thermal aging, *J. Nucl. Mater.* 510 (2018) 382–395.
- [14] M. Honjo, Y. Saito, Numerical simulation of phase separation in Fe–Cr binary and Fe–Cr–Mo ternary alloys with use of the Cahn–Hilliard equation, *ISIJ Int.* 40 (9) (2000) 914–919.
- [15] S. Li, Y. Wang, X. Wang, Influence of Mo Additions on the Mechanical Properties of Cast Duplex Stainless Steels before and after Thermal Aging, *Metals* 9 (3) (2019) 295.
- [16] M.K. Miller, J.M. Hyde, A. Cerezo, G.D.W. Smith, Comparison of low temperature decomposition in Fe–Cr and duplex stainless steels, *Appl. Surf. Sci.* 87–88 (1995) 323–328.
- [17] F. Danoix, P. Auger, Atom probe studies of the Fe–Cr system and stainless steels aged at intermediate temperature: a review, *Mater. Charact.* 44 (1–2) (2000) 177–201.
- [18] V.A. Hosseini, M. Thuvander, S. Wessman, L. Karlsson, Spinodal Decomposition in Functionally Graded Super Duplex Stainless Steel and Weld Metal, *Metallur. Mater. Trans. A* 49 (7) (2018) 2803–2816.
- [19] J. Zhou, J. Odqvist, M. Thuvander, S. Hertzman, P. Hedström, Concurrent phase separation and clustering in the ferrite phase during low temperature stress aging of duplex stainless steel weldments, *Acta Mater.* 60 (16) (2012) 5818–5827.
- [20] V.A. Hosseini, L. Karlsson, D. Engelberg, S. Wessman, Time-temperature-precipitation and property diagrams for super duplex stainless steel weld metals, *Weld, World* (2018).
- [21] V.A. Hosseini, L. Karlsson, C. Örne, P. Reccagni, S. Wessman, D. Engelberg, Functionally Graded Microstructure of Super Duplex Stainless Steel, *Mater. Charact.* 139 (2018) 11.
- [22] G. Chail, P. Kangas, Super and hyper duplex stainless steels: Structures, properties and applications, *Procedia Struct. Integrity* 2 (2016) 1755–1762.
- [23] B. Zhang, Z. Jiang, H. Li, S. Zhang, H. Feng, H. Li, Precipitation behavior and phase transformation of hyper duplex stainless steel UNS S32707 at nose temperature, *Mater. Charact.* 129 (2017) 31–39.
- [24] S.-T. Kim, I.-S. Lee, J.-S. Kim, S.-H. Jang, Y.-S. Park, K.-T. Kim, Y.-S. Kim, Investigation of the localized corrosion associated with phase transformation of tube-to-tube sheet welds of hyper duplex stainless steel in acidified chloride environments, *Corros. Sci.* 64 (2012) 164–173.
- [25] V.A. Hosseini, L. Karlsson, K. Hurtig, I. Choquet, D. Engelberg, M.J. Roy, C. Kumara, A novel arc heat treatment technique for producing graded microstructures through controlled temperature gradients, *Mater. Des.* 121 (2017) 11–23.
- [26] S. Kumar, S. Krisam, A. Jacob, F. Kiraly, A. Keplinger, R. Abart, E. Povoden-Karadeniz, Microstructures and element distributions in an aged hyper duplex stainless steel and corresponding hardness variation, *Mater. Des.* 194 (2020) 108951.
- [27] *Handbook of stainless steel*, Outokumpu Oyj, Finland, 2013.
- [28] V.A. Hosseini, K. Lindgren, M. Thuvander, D. Gonzalez, J. Oliver, L. Karlsson, Nanoscale phase separations in as-fabricated thick super duplex stainless steels, *J. Mater. Sci.* 56 (21) (2021) 12475–12485.
- [29] A. Keplinger, C. Martinez, M. Hausbauer, M. Kapp, Early Stages of Deleterious Phases in Super and Hyper Duplex Stainless Steel and Their Effect on Toughness Frühphasen schädlicher Phasen in Super- und Hyperduplex-Edelstahl und ihr Einfluss auf die Zähigkeit, *BHM Berg- und Hüttenmännische Monatshefte* 165 (1) (2020) 33–39.
- [30] E.M. Cojocar, D. Raducanu, A.N. Vintila, S.S. Alturaihi, N. Serban, A.C. Berbecaru, V.D. Cojocar, Influence of ageing treatment on microstructural and mechanical properties of a solution treated UNS S32750/EN 1.4410/F53 Super Duplex Stainless Steel (SDSS) alloy, *J. Mater. Res. Technol.* 9 (4) (2020) 8592–8605.
- [31] N. Pettersson, S. Wessman, M. Thuvander, P. Hedström, J. Odqvist, R.F.A. Pettersson, S. Hertzman, Nanostructure evolution and mechanical property changes during aging of a super duplex stainless steel at 300°C, *Mater. Sci. Eng., A* 647 (2015) 241–248.
- [32] M. Calcagnotto, D. Ponge, E. Demir, D. Raabe, Orientation gradients and geometrically necessary dislocations in ultrafine grained dual-phase steels studied by 2D and 3D EBSD, *Mater. Sci. Eng., A* 527 (10–11) (2010) 2738–2746.
- [33] A. Dutta, P. Mukherjee, N. Gayathri, S. Dey, S. Neogy, T.K. Roy, Microstructural characterisation of 160 MeV oxygen irradiated niobium, *Phil. Mag.* (2021) 1–22.
- [34] N.K. SHARMA, S. SHEKHAR, User-independent EBSD parameters to study the progress of recovery and recrystallization in Cu–Zn alloy during in situ heating, *J. Microsc.* 264 (3) (2016) 362–369.
- [35] Z.P. Xiong, A.A. Saleh, A.G. Kostychev, E.V. Pereloma, Strain-induced ferrite formation and its effect on mechanical properties of a dual phase steel produced using laboratory simulated strip casting, *J. Alloy. Compd.* 721 (2017) 291–306.
- [36] N. Pettersson, S. Wessman, M. Thuvander, P. Hedström, J. Odqvist, R.F. Pettersson, S. Hertzman, Nanostructure evolution and mechanical property changes during aging of a super duplex stainless steel at 300°C, *Mater. Sci. Eng., A* 647 (2015) 241–248.
- [37] T. SAKAI, Y. SAITO, K. HIRANO, K. KATO, Deformation and recrystallization behavior of low carbon steel in high speed hot rolling, *Trans. Iron Steel Inst. Japan* 28 (12) (1988) 1028–1035.
- [38] T.B. Tavares, D.G. Rodrigues, D.B. Santos, Effect of warm rolling and annealing on microstructure, texture, and mechanical properties of a 2205 duplex stainless steel, *steel research international* 91(4) (2020) 1900543.
- [39] A.V. Ponomareva, A.V. Ruban, B.O. Mukhamedov, I.A. Abrikosov, Effect of multicomponent alloying with Ni, Mn and Mo on phase stability of bcc Fe–Cr alloys, *Acta Mater.* 150 (2018) 117–129.
- [40] C. Pareige, M. Roussel, S. Novy, V. Kuksenko, P. Olsson, C. Domain, P. Pareige, Kinetic study of phase transformation in a highly concentrated Fe–Cr alloy: Monte Carlo simulation versus experiments, *Acta Mater.* 59 (6) (2011) 2404–2411.
- [41] J.-M. Liu, Effect of vacancies on phase separation kinetics of binary alloys: A Monte-Carlo approach, *Scr. Mater.* 37 (5) (1997) 535–541.
- [42] K. Yaldram, K. Binder, Spinodal decomposition of a two-dimensional model alloy with mobile vacancies, *Acta Metall. Mater.* 39 (4) (1991) 707–717.
- [43] Y.-S. Li, S.-X. Li, T.-Y. Zhang, Effect of dislocations on spinodal decomposition in Fe–Cr alloys, *J. Nucl. Mater.* 395 (1–3) (2009) 120–130.
- [44] J. Johansson, M. Odén, X.-H. Zeng, Evolution of the residual stress state in a duplex stainless steel during loading, *Acta Mater.* 47 (9) (1999) 2669–2684.
- [45] X. Xu, J.E. Westraadt, J. Odqvist, T.G.A. Youngs, S.M. King, P. Hedström, Effect of heat treatment above the miscibility gap on nanostructure formation due to spinodal decomposition in Fe–52.85 at.% Cr, *Acta Mater.* 145 (2018) 347–358.
- [46] J. Tian, W. Wang, L. Yin, W. Yan, Y. Shan, K.e. Yang, Three dimensional atom probe and first-principles studies on spinodal decomposition of Cr in a Co-alloyed maraging stainless steel, *Scr. Mater.* 121 (2016) 37–41.
- [47] C.-J. Park, H.-S. Kwon, Effects of aging at 475°C on corrosion properties of tungsten-containing duplex stainless steels, *Corros. Sci.* 44 (12) (2002) 2817–2830.
- [48] R. Badyka, S. Saille, J. Emo, C. Domain, C. Pareige, Effect of Ni, Mo and Mn content on spinodal decomposition kinetics and G-phase precipitation of aged model cast austenitic stainless steels, *J. Nucl. Mater.* 555 (2021) 153123, <https://doi.org/10.1016/j.jnucmat.2021.153123>.
- [49] L. Weber, P.J. Uggowitzer, Partitioning of chromium and molybdenum in super duplex stainless steels with respect to nitrogen and nickel content, *Mater. Sci. Eng., A* 242 (1) (1998) 222–229.
- [50] B. Zhang, H. Li, S. Zhang, Z. Jiang, Y. Lin, H. Feng, H. Zhu, Effect of nitrogen on precipitation behavior of hyper duplex stainless steel S32707, *Mater. Charact.* 175 (2021) 111096.
- [51] T. Bliznuk, M. Mola, E. Polshin, M. Pohl, V. Gavriljuk, Effect of nitrogen on short-range atomic order in the ferritic  $\delta$  phase of a duplex steel, *Mater. Sci. Eng., A* 405 (1) (2005) 11–17.
- [52] D. Garfinkel, J. Poplawsky, W. Guo, G. Young, J. Tucker, Influence of Alloying on  $\alpha$ - $\alpha'$  Phase Separation in Duplex Stainless Steels, 2019.
- [53] T. Zhou, Y.i. Xiong, X. Zha, Y. Yue, Y. Lu, T.-T. He, F.-Z. Ren, E. Rani, H. Singh, J. Kömi, M. Huttula, W. Cao, Hot-deformation-induced structural and mechanical properties of Ce-modified SAF 2507 super duplex stainless steel, *J. Mater. Res. Technol.* 9 (4) (2020) 8379–8390.
- [54] L. Duprez, B.C. De Cooman, N. Akdut, Deformation behaviour of duplex stainless steel during industrial hot rolling, *Steel research* 73 (12) (2002) 531–538.
- [55] N. Holländer Pettersson, D. Lindell, F. Lindberg, A. Borgenstam, Formation of Chromium Nitride and Intragranular Austenite in a Super Duplex Stainless Steel, *Metallur. Mater. Trans. A* 50 (12) (2019) 5594–5601.
- [56] N. Pettersson, R.F.A. Pettersson, S. Wessman, Precipitation of chromium nitrides in the super duplex stainless steel 2507, *Metallur. Mater. Trans. A* 46 (3) (2015) 1062–1072.
- [57] P. Hedström, F. Huyan, J. Zhou, S. Wessman, M. Thuvander, J. Odqvist, The 475°C embrittlement in Fe–20Cr and Fe–20Cr–X (X= Ni, Cu, Mn) alloys studied by mechanical testing and atom probe tomography, *Mater. Sci. Eng., A* 574 (2013) 123–129.
- [58] I.S. Golovin, V.I. Sarrak, S.O. Suvorova, Influence of carbon and nitrogen on solid solution decay, *Metall. Trans. A* 23 (9) (1992) 2567–2579.